# Management of light absorption in extraordinary optical transmission based ultra-thin-film tandem solar cells

Kishwar Mashooq and Muhammad Anisuzzaman Talukder

---

### Articles you may be interested in

Properties of reactively sputtered oxygenated cadmium sulfide (CdS:O) and their impact on CdTe solar cell performance
J. Vac. Sci. Technol. A **33**, 021203 (2015); 10.1116/1.4903214

Influence of different sulfur to selenium ratios on the structural and electronic properties of Cu(In,Ga)(S,Se)2 thin films and solar cells formed by the stacked elemental layer process
J. Appl. Phys. **116**, 174503 (2014); 10.1063/1.4900991

The impact of oxygen incorporation during intrinsic ZnO sputtering on the performance of Cu(In,Ga)Se2 thin film solar cells
Appl. Phys. Lett. **105**, 083906 (2014); 10.1063/1.4894214

Electron-beam-induced current at absorber back surfaces of Cu(In,Ga)Se2 thin-film solar cells
J. Appl. Phys. **115**, 014504 (2014); 10.1063/1.4858393

Size-quantized CdS films in thin film CuInS 2 solar cells
Appl. Phys. Lett. **73**, 3135 (1998); 10.1063/1.122697

---

# Management of light absorption in extraordinary optical transmission based ultra-thin-film tandem solar cells

Kishwar Mashooq and Muhammad Anisuzzaman Talukder[a)]
*Department of Electrical and Electronic Engineering, Bangladesh University of Engineering and Technology, Dhaka 1205, Bangladesh*

Although ultra-thin-film solar cells can be attractive in reducing the cost, they suffer from low absorption as the thickness of the active layer is usually much smaller than the wavelength of incident light. Different nano-photonic techniques, including plasmonic structures, are being explored to increase the light absorption in ultra-thin-film solar cells. More than one layer of active materials with different energy bandgaps can be used in tandem to increase the light absorption as well. However, due to different amount of light absorption in different active layers, photo-generated currents in different active layers will not be the same. The current mismatch between the tandem layers makes them ineffective in increasing the efficiency. In this work, we investigate the light absorption properties of tandem solar cells with two ultra-thin active layers working as two subcells and a metal layer with periodically perforated holes in-between the two subcells. While the metal layer helps to overcome the current mismatch, the periodic holes increase the absorption of incident light by helping extraordinary optical transmission of the incident light from the top to the bottom subcell, and by coupling the incident light to plasmonic and photonic modes within ultra-thin active layers. We extensively study the effects of the geometry of holes in the intermediate metal layer on the light absorption properties of tandem solar cells with ultra-thin active layers. We also study how different metals in the intermediate layer affect the light absorption; how the geometry of holes in the intermediate layer affects the absorption when the active layer materials are changed; and how the intermediate metal layer affects the collection of photo-generated electron-hole pairs at the terminals. We find that in a solar cell with 6,6-phenyl C61-butyric acid methyl ester top subcell and copper indium gallium selenide bottom subcell, if the periodic holes in the metal layer are square or polygon, total absorption remains approximately the same. However, the total absorption suffers significantly if the holes are triangle. The transmission spectra of incident light into the bottom subcell, and hence the absorption, change significantly for square and circle holes if the active materials change to cadmium selenide (CdSe) and cadmium telluride (CdTe) in the top and bottom subcells, respectively. Although the intermediate metal layer may induce electron-hole pair recombination due to surface defects, the short-circuit current density of an ultra-thin plasmonic solar cell with an intermediate metal layer with two-dimensional hole array is >9% of that of a structure without the intermediate metal layer. *Published by AIP Publishing.* [http://dx.doi.org/10.1063/1.4949588]

## I. INTRODUCTION

In modern world, one of the major challenges that our society faces is to provide low-cost and environment-friendly energy sources because of the increasing demand of energy. The average usage of energy in current world is ∼2206 TW.[1] The incident solar radiation intensity on earth is 0.925 kW/m$^2$. Therefore, the amount of available solar radiation on earth is ∼$1.5 \times 10^5$ TW.[2] However, the use of solar cells is not as widespread as one would expect mainly due to their high cost and the low efficiency. The maximum portion of the production cost of solar cells is due to the material cost of active regions. The material cost, and hence the solar cell cost, can be significantly reduced by decreasing the thickness of the active region. However, the decrease in thickness of the active region comes with the adverse effect of a decrease in absorption of incident solar energy, and hence a decrease in efficiency.

Different nano-photonic techniques are being explored to increase the light absorption in thin-film and ultra-thin-film solar cells so that the cost can be reduced without sacrificing efficiency. Till date, a number of structures have been used that are capable of coupling the incident light to surface modes such as surface plasmon polaritons (SPPs) and localized surface plasmons (LSPs), and different photonic modes so that light can be confined in a sub-wavelength dimensional structure. The structures mainly use nano-structures and gratings of metal and dielectric material in different layers of solar cells.[3–15]

Extraordinary optical transmission (EOT) is a phenomenon of enhanced optical transmission through a periodically perforated sub-wavelength metal hole array structure.[16,17] EOT was discovered by Ebbesen in 1998, and since then has been used in applications such as in designing left handed metamaterials and EOT based sensors.[16,18–20] The transmission spectra

a)anis@eee.buet.ac.bd

of EOT can be controlled by changing the different dimensional parameters of the periodic hole array. Additionally, EOT inherently involves excitation of different surface modes such as SPPs and localized cut-off resonance modes within holes. Therefore, EOT can be a promising technique to increase the light absorption in thin-film and ultra-thin-film solar cells, especially when more than one ultra-thin active layer is used in tandem. A metal hole array can be placed between the subcells, and cut-off wavelength for transmission can be controlled to optimize the solar absorption in both the top and bottom subcells. Additionally, the metal layer can be used to overcome the problem of current mismatch in a tandem solar cell.

Recently, there has been a proposal of EOT based solar cell by Zhang *et al.*[21] In the proposal, a metal layer with a two-dimensional hole array (2DHA) with square holes has been used between 6,6-phenyl C61-butyric acid methyl ester (PCBM) top subcell and copper indium gallium selenide (CIGS) bottom subcell so that EOT can be used to increase solar absorption. Zhang *et al.* discussed how the absorption of incident solar radiation can be optimized by changing the dimensions of square hole array in-between the top PCBM and the bottom CIGS subcells.[21] However, the absorption of incident light in an EOT based solar cell will depend also on the shape of the holes, the metal used in the intermediate layer, and the materials used as the top and the bottom subcells. In this work, we investigate the effects of the geometry of holes on the absorption of incident light in EOT based ultra-thin-film tandem solar cells. We investigate the effects of the change of the metal in the intermediate layer. We investigate the effects when active materials are changed and how the intermediate layer with periodic 2DHA should be designed for different active materials. We also investigate the effect of the metal layer in the collection of photo-generated electron-hole pairs. We find that the transmission spectra into the bottom subcell significantly change as the hole shape is changed from triangle to square or polygon such as hexagon, octagon, or circle. The total absorption in an EOT based tandem solar cell with PCBM top and CIGS bottom subcells remains approximately the same as the number of arms of holes increases to $\geq 4$. However, the selection of hole geometry can be critical for different active materials. We find that while the total absorption is almost the same with intermediate square and circle hole arrays in a tandem solar cell with PCBM top and CIGS bottom active layers, the total absorption is much greater in a tandem solar cell with cadmium selenide (CdSe) top and cadmium telluride (CdTe) bottom subcells with intermediate circle hole array than that with square hole array. The intermediate metal layer may increase the recombination rate of photo-generated electron-hole pairs; however, the short circuit current density of the solar cell is still much greater than that without the intermediate metal layer.

The rest of the paper is organized as follows: In Sec. II, we present the structure of EOT based tandem solar cells. In Sec. III, we discuss the simulation approach and methodology of investigation. In Sec. IV, we present and discuss the light transmission and absorption characteristics with different shapes of holes in the hole array. In Sec. V, we investigate the effects of different metals used in the intermediate layer with hole array. In Section VI, we investigate the effects of different active materials used as subcells in EOT based tandem solar cells and how the intermediate layer structure should be designed for different active material systems. In Sec. VII, we calculate the short-circuit current density and investigate the effects of the intermediate metal layer. In Sec. VIII, we draw conclusions on the findings.

## II. EOT BASED SOLAR CELL STRUCTURE

A schematic illustration of an EOT based ultra-thin-film tandem solar cell is given in Fig. 1. The structure in Fig. 1 is similar to that discussed in Ref. 21. In Fig. 1, a CIGS layer of 100 nm is used as the bottom subcell. A thin indium tin oxide (ITO) layer of 10 nm is grown on the CIGS layer. A-50-nm silver (Ag) layer with periodically perforated holes is placed on the ITO layer. Then, a 100-nm-PCBM layer on the Ag layer is used as the top subcell. In this work, we change the geometry and dimensions of holes in the Ag layer, the metal in the intermediate layer, and the materials of the top and bottom subcells.

In practice, a solar cell will have additional layers such as a metal back-contact layer at the bottom, an anti-reflection coating layer on the top of the PCBM layer, and metal fingers on the anti-reflection coating layer. While the metal back-contact layer is necessary for collection of photo-generated carriers, it also helps to increase the light absorption by increasing the path length as the incident light bounces back.[22] The anti-reflection coating layer on the top increases the coupling of the incident light to the solar cell.[23] The metal fingers on the top of anti-reflection coating layer create a shaded region on the active layer, and thereby reduce the light absorption by ~10%.[24] The effects of the metal back-contact layer, the anti-reflection coating layer, and the metal fingers are well known and have been investigated in detail.[22–24] Therefore, we do not include these additional layers in the structure shown in Fig. 1; rather, we investigate a structure, which is basically important for the EOT based tandem solar cells.

## III. SIMULATION APPROACH

In order to investigate the dynamics of the incident light on an EOT based ultra-thin-film tandem solar cell, we solve Maxwell's equations using a full-field vectorial finite difference time domain (FDTD) technique. A broadband plane
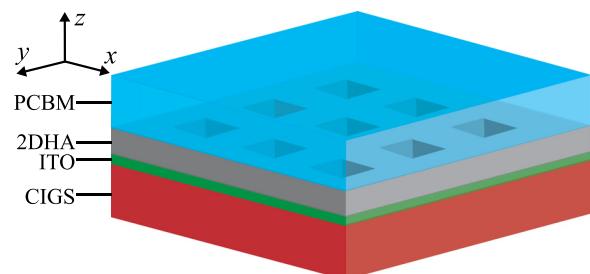


FIG. 1. Schematic illustration of an EOT based ultra-thin-film tandem solar cell.
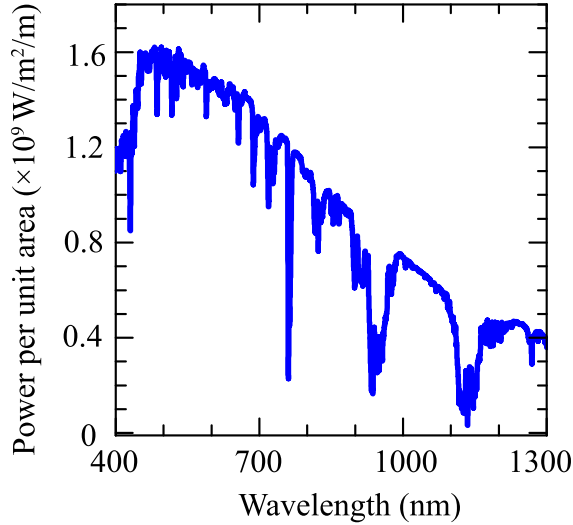
FIG. 2. AM 1.5 solar spectra.

wave with a bandwidth of 400–1300 nm is normally incident on the structure. The incident light is normalized by the AM 1.5 solar spectra, as given in Fig. 2. The light source is placed at a sufficient height of 250 nm from the top surface to minimize diffraction effects. Since the structure shown in Fig. 1 is periodic in both the $x$- and $y$-directions, we consider only one period of the structure and apply periodic boundary conditions in both the $x$- and $y$-directions. By contrast, we apply a perfectly matched layer boundary condition in the $z$-direction.

In this work, we calculate the transmission spectra of the incident light into the bottom subcell. We calculate the normalized transmission $T(\lambda)$ through the $x$-$y$ plane by

$$T(\lambda) = \frac{\int \mathrm{Re}\left[\vec{S}_m(\lambda)\right] \cdot \vec{ds}}{\int \mathrm{Re}\left[\vec{S}_s(\lambda)\right] \cdot \vec{ds}}, \qquad (1)$$

where $\vec{S}_m(\lambda)$ and $\vec{S}_s(\lambda)$ are the poynting vectors in the $x$-$y$ planes at the metal-ITO layer interface and at the source, respectively, and $\vec{ds}$ is the surface normal. The total transmission is calculated by integrating $T(\lambda)$ over the bandwidth

of the incident light. The power absorbed at a position at a frequency is calculated using $-\frac{1}{2}\omega|\vec{E}|^2\mathrm{Im}(\varepsilon)$, where $\omega$ is the angular frequency, $\vec{E}$ is the steady-state electric field, and $\varepsilon$ is the dielectric constant of the material at the position. The total power absorbed is calculated by integrating the power absorbed at a position at a frequency over the structure and over the bandwidth of the source.

In simulation, we used grid sizes that are much smaller than the feature sizes so that an insufficient density of mesh grids does not induce discontinuous or divergent electromagnetic field distribution and hence inaccurate results. We have checked the accuracy and convergence of results by increasing the number of grid points twice at each step until there is no noticeable change in the results. In particular, triangle and square holes in 2DHA have sharp corners that have to be properly defined in the simulation. We have used a uniform meshing of 1.5 nm and 2.5 nm in all directions for triangle and square 2DHA, respectively, where triangle and square holes have arms of lengths of 228 nm and 150 nm, respectively. In Figs. 3(a) and 3(b), we show the grided material index of structures with triangle and square holes for a wavelength of 1144 nm. In Fig. 3(c), we show an enlarged view of grided material index and mesh-grids around the corner of a triangle hole, and in Fig. 3(d), we show an example of the electric field distribution for the incident light around the edge of a triangle hole. In Fig. 3(e), we show an enlarged view of grided material index and mesh-grids around the corner of a square hole, and in Fig. 3(f), we show an example of the electric field distribution for the incident light around the edge of a square hole. We note that the sharp corners in triangle and square holes are properly defined and the electric fields are continuous even at the edges of triangle and square holes.

## IV. EFFECTS OF GEOMETRY OF HOLES IN 2DHA

In this section, we investigate the effects of geometry of holes in 2DHA on light absorption in ultra-thin-film tandem solar cells. In particular, we discuss the EOT through triangle, square, and regular polygon hole arrays. In Fig. 4, we show the $x$-$y$ cross-sections of one period of the structures
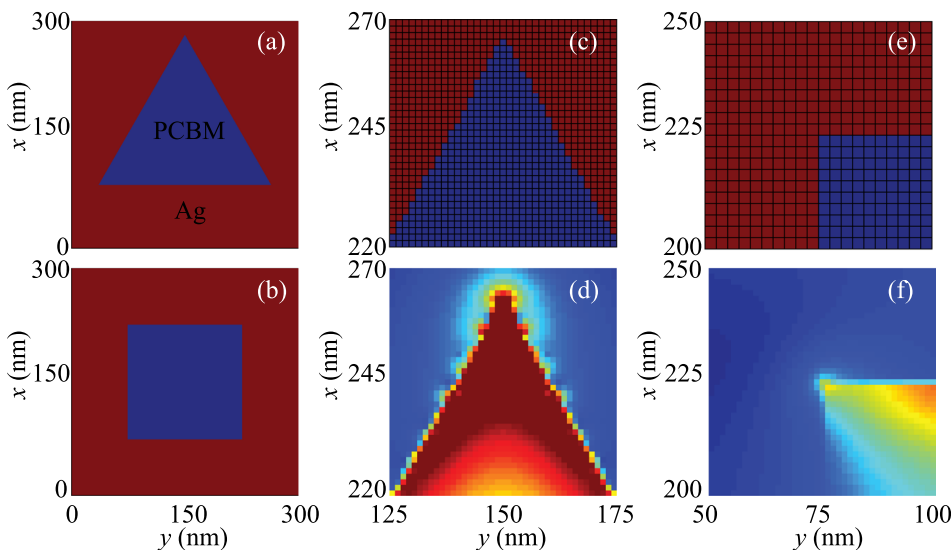


FIG. 3. Material index in the $x$-$y$ cross-section through the center of holes in (a) triangle 2DHA and (b) square 2DHA. (c) Enlarged portion of material index and mesh-grids around the corner of a hole in a triangle 2DHA, (d) enlarged view of electric field profile for incident light around the corner of a hole in triangle 2DHA, (e) enlarged portion of material index and mesh-grids around the corner of a hole in a square 2DHA, and (f) enlarged view of electric field profile for incident light around the corner of a hole in square 2DHA.
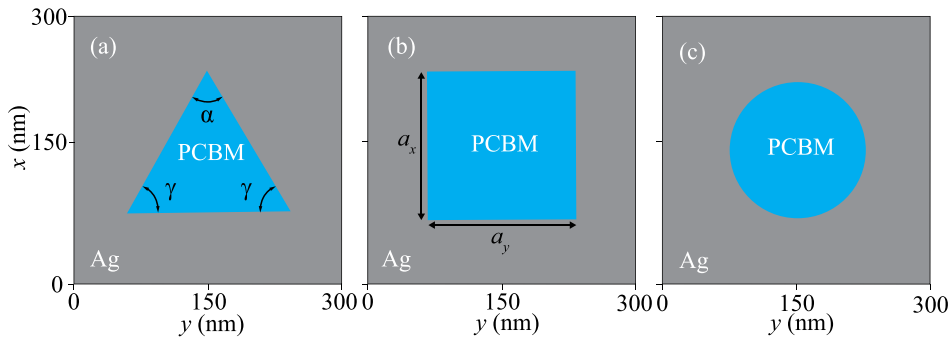
FIG. 4. Schematic illustrations of cross-sections of one period of solar cells in the *x-y* plane through the center of holes for (a) triangle 2DHA, (b) square 2DHA, and (c) circle 2DHA.

through the center of the holes when the holes are triangle, square, and circle.

The EOT mainly depends on the excitation of SPP modes in the metal-dielectric interface and localized cut-off resonance modes within holes.[16] The SPPs depend on the shape of the holes to achieve phase-matching condition for the in-plane wavevector to excite the surface plasmons. A cut-off resonance mode can be described as a Fabry-Perot mode inside a hole in 2DHA, which occurs close to the condition of vanishing propagation constant. For example, the propagation constant of a TE or a TM mode of a rectangular hole in a perfect electric conductor can be defined by[25]

$$\beta = \pi \sqrt{\left(\frac{2}{\lambda}\right)^2 - \left(\frac{1}{a}\right)^2}, \qquad (2)$$

where $\beta$ is the propagation constant, $\lambda$ is the wavelength, and $a$ is the length of the rectangular hole. In this case, the cut-off wavelength occurs at $\lambda = 2a$, which is known as Rayleigh's criterion, where the propagation constant becomes zero. While the cut-off resonance modes do not depend on parallel wavevectors, they strongly depend on the geometry and size of holes.

### A. Triangle holes in 2DHA

The transmission characteristics of a 2DHA with triangle holes sensitively depend on the value of the smallest angle of the triangle if the area is fixed. To find out the effects of an angle in a triangle on EOT, we assume an isosceles triangle with the smallest angle $\alpha$ and two equal angles $\gamma$, where $\alpha \le \gamma$, as shown in Fig. 4. As the value of the smallest angle decreases, the localized field increases due to enhanced coupling of the incident light to cut-off resonance modes. Since the lengths of the arms that make an angle increase with the decrease of that angle if the area is fixed, the distance between the tip of that angle and the opposite arm increases. Therefore, the light coupled in the resonant cut-off mode is red-shifted with the decrease of the smallest angle.

In Fig. 5, we show the transmission spectra through a triangle hole array into the bottom subcell of an ultra-thin-film tandem solar cell with PCBM top and CIGS bottom active layers for different values of the smallest angle in triangles. We show the transmission spectra for TE- and TM-polarized incident light in Figs. 5(a) and 5(b), respectively. We note that the transmission peaks in the shorter wavelengths are relatively unchanged when the value of the smallest angle changes.

However, the peak in the longer wavelength is blue-shifted as the value of smallest angle increases. Therefore, Figs. 5(a) and 5(b) show that the transmission to the bottom subcell, and hence the light absorption in the solar cell, can be changed by changing the angle of a triangle hole. In the coordinate system defined in Fig. 1, the TE-polarized light has an electric field polarized in the *x*-direction, but the TM-polarized light has an electric field polarized in the *y*-direction. Depending on the orientation of the triangle holes in the *x-y* plane, the excitation of localized modes changes due to the TE- and TM-polarized light. Therefore, we note that the transmission spectra for the TE- and TM-polarized incident light are different in Figs. 5(a) and 5(b).

In Figs. 5(c)–5(e), we show the normalized electric field profiles in the *x-y* plane at the interface of the metal-ITO layer at the wavelengths of peak transmission for the TE-polarized incident light. Similarly, in Figs. 5(f)–5(h), we show the normalized electric field profiles in the *x-y* plane at the interface of the metal-ITO layer at the wavelengths of peak transmission for the TM-polarized incident light. From the field profiles, we note that the transmission peaks through a triangle hole array are due to the excitation of the cut-off resonance modes.

As the excitation mechanism of EOT through a triangle 2DHA is mainly the localized cut-off resonance modes as shown in Fig. 5, it does not necessarily depend on the parallel wave vectors of the incident light. Therefore, the transmission through a metal layer with a triangle hole array is relatively independent of the incidence angle of light. This property is important for designing solar cells as the solar radiation may not always be incident normally. If the excitation mechanism of EOT in a structure is mainly the surface modes such as SPPs, the transmission through a 2DHA will suffer in case of inclined light incidence as the surface modes strongly depend on parallel wave vectors of the incident light.

### B. Square holes in 2DHA

When the holes in a 2DHA are square, i.e., the angles between neighboring arms are 90°, SPP resonances are much stronger than that when the holes in a 2DHA are triangle. In Fig. 6(a), we show the transmission spectra of the incident light into the bottom subcell of an ultra-thin-film tandem solar cell with PCBM top and CIGS bottom active layers when the holes in a 2DHA are square. The transmission spectra will be the same for both TE- and TM-polarized incident light due to the symmetry of geometry of holes. We note that the transmission through a square hole array increases and
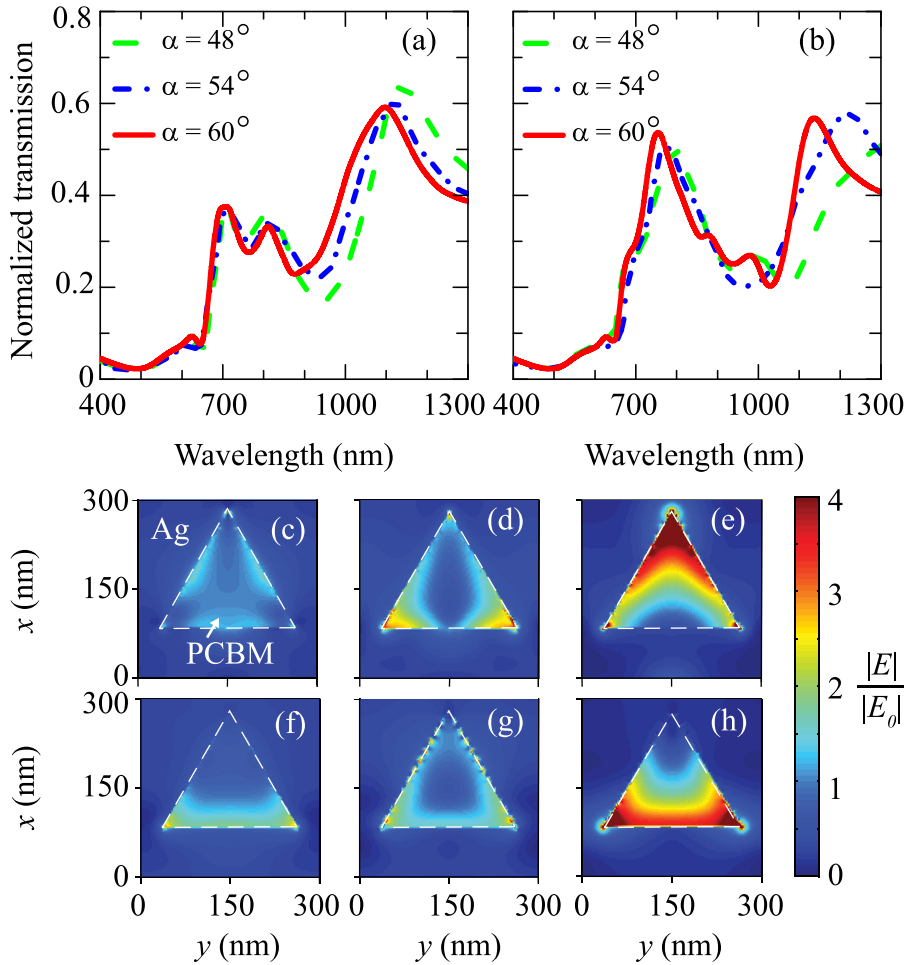
FIG. 5. Normalized transmission spectra into the bottom subcell through a 2DHA with triangle holes when the normally incident light is (a) TE-polarized and (b) TM-polarized. Normalized electric field profile ($|E|/|E_0|$) in the $x$-$y$ plane at the metal-ITO layer interface for normally incident TE-polarized light with wavelengths of (c) 698 nm, (d) 810 nm, and (e) 1100 nm. $|E|/|E_0|$ in the $x$-$y$ plane at the metal-ITO layer interface for normally incident TM-polarized light with wavelengths of (f) 747 nm, (g) 915 nm, and (h) 1144 nm. In each case, the area of triangles is fixed at 22 500 nm$^2$.

blue-shifts from that through a triangle hole array. The first two peaks in the transmission profile at 700 nm and 764 nm are largely due to the excitation of SPPs, whereas the third peak at 914 nm is mainly due to the excitation of the cut-off resonance modes.

In Figs. 6(b)–6(e), we present two dimensional field profiles in both the $x$-$y$ and $x$-$z$ planes at the wavelengths of second and third peaks of transmission spectra. In Fig. 6(b), we present the normalized electric field profile in the $x$-$y$ plane at

the interface of metal-ITO layer for an incident light of 764 nm wavelength. We note that the incident light strongly couples to SPPs at 764 nm. The excitation of SPPs at 764 nm is also clear in Fig. 6(c), where we plot the normalized electric field profile in the $x$-$z$ plane through the center of the hole. At the same time, we note that the cut-off resonance is insignificant at 764 nm. By contrast, the incident light is strongly coupled to localized cut-off resonance when the wavelength is 914 nm, as shown in Fig. 6(d). Strong light coupling to cut-off
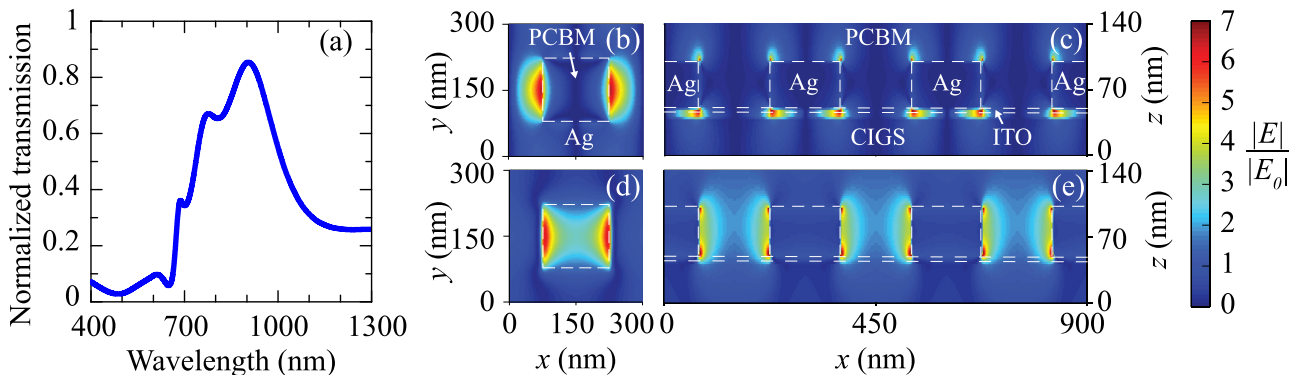


FIG. 6. (a) Normalized transmission spectra into the bottom subcell through a 2DHA with square holes for normally incident TE-polarized light. Normalized electric field profile ($|E|/|E_0|$) for normally incident TE-polarized light of wavelength of 764 nm in the (b) $x$-$y$ plane at the interface of metal-ITO layer and (c) $x$-$z$ plane through the center of the hole. $|E|/|E_0|$ for normally incident TE-polarized light of wavelength of 914 nm in the (d) $x$-$y$ plane at the interface of metal-ITO layer and (e) $x$-$z$ plane through the center of the hole. In each case, the area of square holes is fixed at 22 500 nm$^2$.

resonance at 914 nm is also clear in Fig. 6(e), where we plot the normalized electric field profile in the *x-z* plane through the center of the hole. At the same time, we note that the SPPs are not excited at 914 nm.

The excitation mechanisms of EOT, and hence the transmission spectra, depend on the dimensional parameters of 2DHA. In Fig. 7, we show the change in the transmission spectra when the periodicity and the ratio of the lengths of arms of square holes in a 2DHA change. In Fig. 7(a), we note that the transmission spectra blue shift as the periodicity decreases. The change in transmission peak with the change in periodicity is given by[26]

$$\lambda_{\max} = \frac{2\pi}{G_{mn}} \sqrt{\frac{\varepsilon_d \varepsilon_m}{\varepsilon_d + \varepsilon_m}}, \qquad (3)$$

where $\varepsilon_d$ and $\varepsilon_m$ are the dielectric constants of dielectric active layer and metal layer, respectively, and $G_{mn}$ is the reciprocal vector, where $m$ and $n$ are the directions of propagation. The parameter $G_{mn}$ is inversely proportional to the periodicity of the unit cell. Therefore, the transmission spectra blue shift when the periodicity of 2DHA decreases. As the lengths of arms of holes in an array change, the cut-off resonance changes as well. In Fig. 7(b), we note that the transmission peak at 914 nm with $a_x/a_y = 1$ is red-shifted for $a_x/a_y < 1$ and blue-shifted for $a_x/a_y > 1$, where $a_x$ and $a_y$ are the lengths of holes in the *x*- and *y*-directions. This shift of transmission is due to the change in coupling of modes with respect to the change in hole dimensions in 2DHA.

### C. Regular polygon holes in 2DHA

Now, as the number of arms in a regular polygon increases to more than 4, the angle between any two neighboring arms becomes greater than 90°. As a result, the incident light couples less to the localized modes but more to the surface modes. Therefore, the SPPs become the dominant excitation mechanism of EOT as the number of arms in the holes becomes greater than 4. In Fig. 8(a), we show the transmission spectra into the bottom subcell of an ultra-thin-film tandem solar cell with PCBM top and CIGS bottom active layers when the holes in a 2DHA are hexagon, octagon, and circle. The transmission spectra will be the same for both TE- and

TM-polarized incident light due to the symmetry of geometry of holes. We note that the peak positions in the transmission spectra do not change much for hexagon, octagon, and circle holes. We find that the peaks in the transmission spectra through a 2DHA with regular polygon holes with a number of arms greater than 4 blue-shift with respect to that through a 2DHA with triangle or square holes. This blue-shift occurs as the dominant modes in a polygon with a number of arms greater than 4 change from cut-off resonances to SPPs, and for the dimension of the holes and the index of materials in the structure, an SPP resonance is at a shorter wavelength than that of cut-off resonance.

In Figs. 8(b)–8(e), we show the normalized electric field profiles in the *x-y* and the *x-z* planes when the holes in a 2DHA are circle. We show the normalized electric field profile for 716 nm incident light in the *x-y* plane at the interface of the metal-ITO layer and in the *x-z* plane through the center of the hole in Figs. 8(b) and 8(c), respectively. We note that the SPPs are excited. We show the normalized electric field profile for 885 nm incident light in the *x-y* plane at the interface of metal-ITO layer and in the *x-z* plane through the center of the hole in Figs. 8(d) and 8(e), respectively. We note that the SPPs are excited in this case too. However, the SPPs are stronger at 885 nm than that at 716 nm.

Since the geometry of holes changes the transmission spectra into the bottom subcell of an ultra-thin-film tandem solar cell, the absorption characteristics will change as well. We have calculated the total absorption in both the top and bottom subcells when the geometry of holes changes and the results are given in Fig. 9(a). The total absorption is calculated assuming 50% TM- and 50% TE-polarized light in incident solar radiation and weighting by the AM 1.5 solar spectra. We note that the total absorption in the top subcell is approximately the same with any geometry of holes. However, the total absorption in the bottom subcell changes significantly with the geometry of holes in 2DHA.

In Fig. 9(b), we show the total absorption when the area of square holes in a 2DHA changes. While the light transmission to the bottom subcell increases with the increase in area of the holes, the absorption in the top subcell decreases. Therefore, if the transmission to the bottom subcell increases too much by increasing the hole area, the total absorption of
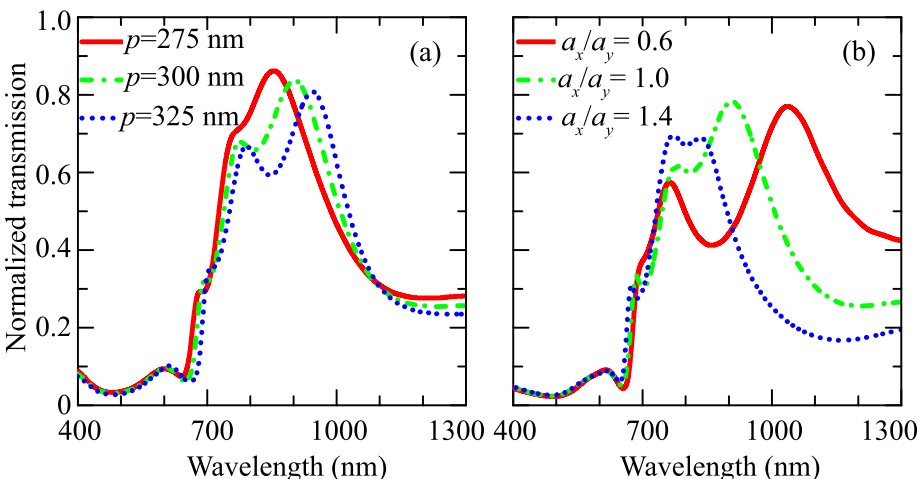


FIG. 7. Normalized transmission spectra into the bottom subcell through a 2DHA with square holes for normally incident TE-polarized light for (a) different periodicities (*p*) of holes and (b) different ratios of the lengths of holes in the *x*- and *y*-directions ($a_x/a_y$). In each case, the area of square holes is fixed at 22 500 nm$^2$.
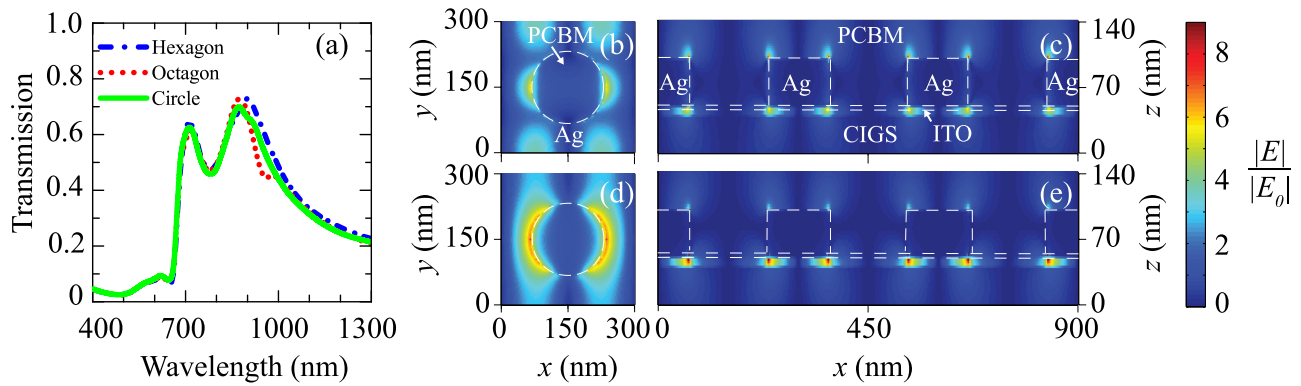
FIG. 8. (a) Normalized transmission spectra into the bottom subcell through a 2DHA with hexagon, octagon, and circle holes for normally incident TE-polarized light. Normalized electric field profile ($|E|/|E_0|$) for normally incident TE-polarized light of wavelength of 716 nm in the (b) x-y plane at the interface of metal-ITO layer and (c) x-z plane through the center of the hole in a structure with circle holes in the 2DHA. $|E|/|E_0|$ for normally incident TE-polarized light of wavelength of 885 nm in the (d) x-y plane at the interface of metal-ITO layer and (e) x-z plane through the center of the hole in a structure with circle holes in the 2DHA. In each case, the area of holes is fixed at 22 500 nm$^2$.
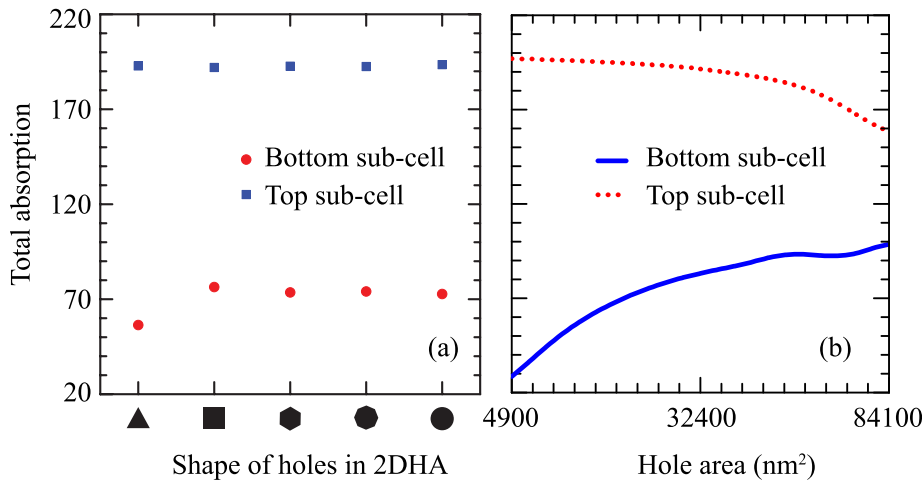


FIG. 9. Total absorption in the top and the bottom subcells for (a) different geometry of holes in the 2DHA and (b) change in area of holes in square 2DHA.

the solar cell may decrease. In this work, with PCBM top and CIGS bottom subcells, we find that the absorption is maximum when the area of the square hole is 36 400 nm$^2$.

## V. METALS IN 2DHA

Metals like silver, gold, and copper can be used as the intermediate layer with 2DHA for EOT in tandem solar cells. In Fig. 10(a), we plot the normalized transmission spectra into the bottom subcell when silver, gold, and copper are used for 2DHA between PCBM and CIGS subcells. We note that the transmission through a silver 2DHA is greater than that through a gold or a copper 2DHA. In Fig. 10(b), we plot the absorption in silver, gold, and copper intermediate layers with 2DHA. We note that the loss due to absorption in the intermediate metal layer is smaller when silver is used than that when gold and copper are used. The greater loss in gold and copper than that in silver is mainly due to the greater interband absorption of incident photons in gold and copper within the spectra of incident solar radiation.[27] The absorption characteristics of these metals can be manifested in their complex dielectric constant ($\varepsilon$). In Figs. 10(c) and 10(d), we plot the real ($\varepsilon_r$) and imaginary ($\varepsilon_i$) parts of the complex dielectric constants of gold, copper, and silver. While the real part represents the amount of polarization, the imaginary

part represents the losses encountered in polarizing the materials. We note that $\varepsilon_i$ of silver is smaller than that of gold and copper throughout the spectra of incident solar radiation. Therefore, in an EOT based ultra-thin-film tandem solar cell, silver will be the metal of choice for 2DHA between the active layers.

## VI. DIFFERENT MATERIALS FOR SUBCELLS

In a conventional tandem solar cell with two active layers, the material that has the higher energy bandgap is placed on top of the other. The purpose of placing the material with the higher energy bandgap material on the top is to absorb high energy photons in the top subcell and to absorb low energy photons in the bottom subcell that are not absorbed in the top subcell.

Currently, common inorganic materials used in thin-film and ultra-thin-film tandem solar cells are CIGS, Cd based materials, e.g., cadmium telluride (CdTe), cadmium sulfide (CdS), and cadmium selenide (CdSe), amorphous silicon (A-Si), and micro-crystalline silicon ($\mu$C-Si).[28] The periodically perforated metal 2DHA between two layers of a tandem solar cell will act as a high pass filter for the incident solar spectrum. The cut-off wavelength of this filter is of great significance in designing an EOT based tandem solar cell. The
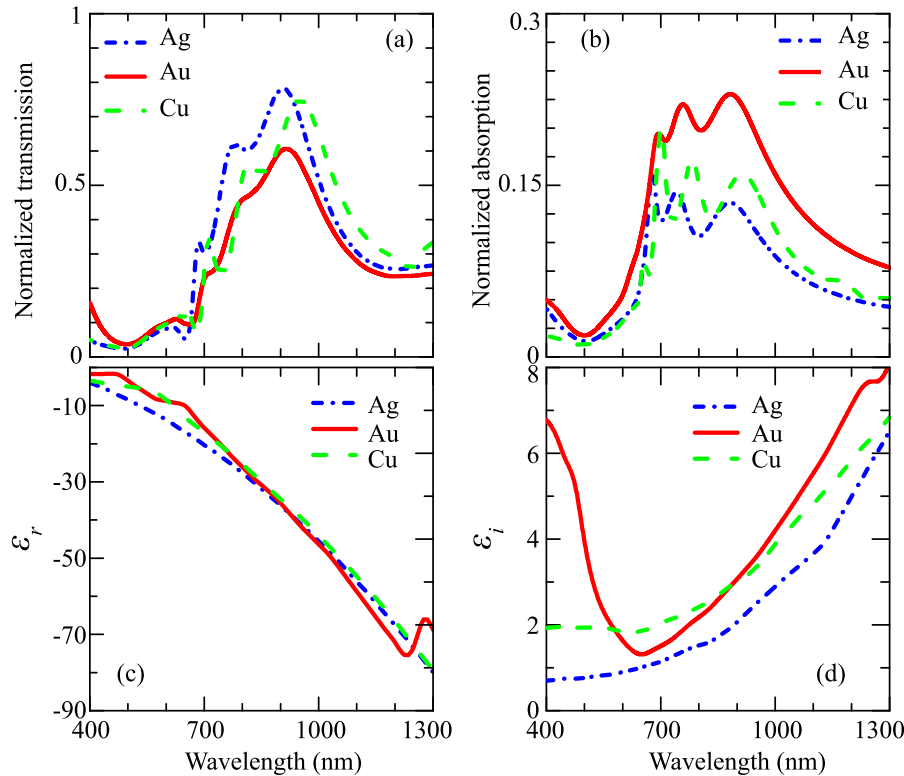
FIG. 10. (a) Normalized transmission spectra through a 2DHA with square holes for silver (Ag), gold (Au), and copper (Cu), (b) normalized absorption spectra in Ag, Au, and Cu where they are used as the metal for 2DHA with square holes, (c) real part of dielectric constant ($\varepsilon_r$) for Ag, Au, and Cu, and (d) imaginary part of dielectric constant ($\varepsilon_i$) for Ag, Au, and Cu.

cut-off wavelength can be controlled by changing the materials of both top and bottom layers, metals in 2DHA, and the geometry of holes in 2DHA. The bulk absorption of the top subcell material can be used as a design guideline for EOT based tandem solar cells. From Fig. 11, we note that the bulk absorption in PCBM is insignificant beyond 600 nm wavelength. By contrast, CIGS can significantly absorb even at 1000 nm wavelength. Therefore, in a tandem solar cell, PCBM can be used as the top subcell while CIGS can be used as the bottom subcell. The intermediate metal 2DHA should be designed with a cut-off wavelength ∼600 nm. In the designs in this work with PCBM as the top layer and CIGS as the bottom layer, the cut-off wavelength has been ∼650 nm.
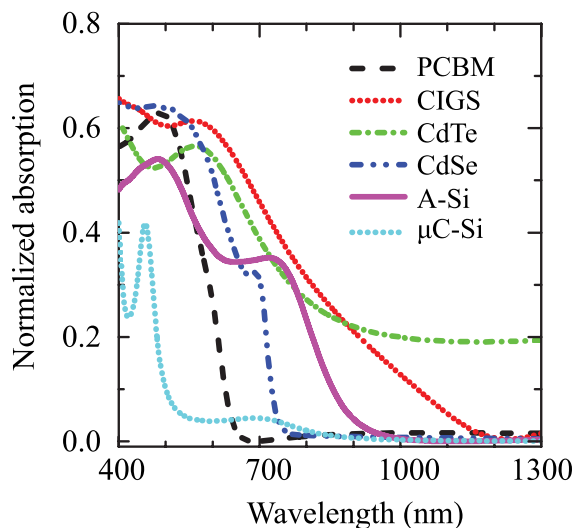


FIG. 11. Bulk absorption spectra of different solar cell materials.

In an EOT based solar cell, the geometry of holes of a 2DHA can make a seemingly unimpressive solar cell material an excellent candidate for solar energy absorption. For example, CdSe/CdTe based ultra-thin-film tandem solar cell with a 2DHA with square holes has a cut-off wavelength of ∼1050 nm, which will not lead to efficient absorption of incident solar energy. However, if circle holes are used, the cut-off wavelength is ∼850 nm, as shown in Fig. 12(a), which will lead to significant absorption of incident solar energy. When square 2DHA is used in a CdSe/CdTe based ultra-thin-film solar cell, we note a strong excitation of cut-off resonance modes and a weak excitation of SPP modes as well, as shown in Fig. 12(b). However, when the holes are circle in 2DHA, the resonant mode is dominantly SPP, as shown in Fig. 12(c). Due to the greater dielectric constant of CdSe than that of PCBM, the cut-off resonance in a CdSe/CdTe solar cell is at a much greater wavelength than that in a PCBM/CIGS solar cell, and there is a huge blue-shift when the resonance changes from cut-off to SPP as the holes change from square to circle in the intermediate metal layer.

## VII. SHORT-CIRCUIT CURRENT DENSITY

Till now, we find that the intermediate metal layer with a 2DHA between two ultra-thin subcells of a solar cell can increase the light absorption. However, the increase in light absorption will be reflected in the performance of the solar cell if absorbed photons can convert into electron-hole pairs that are collected successfully at the terminals. Therefore, in this section, we calculate the short-circuit current density ($J_{sc}$) and investigate if there are effects on the collection of photo-generated carriers due to the intermediate metal layer. In general, in an ultra-thin active layer, all photo-generated electron-hole pairs can be approximated to be collected at
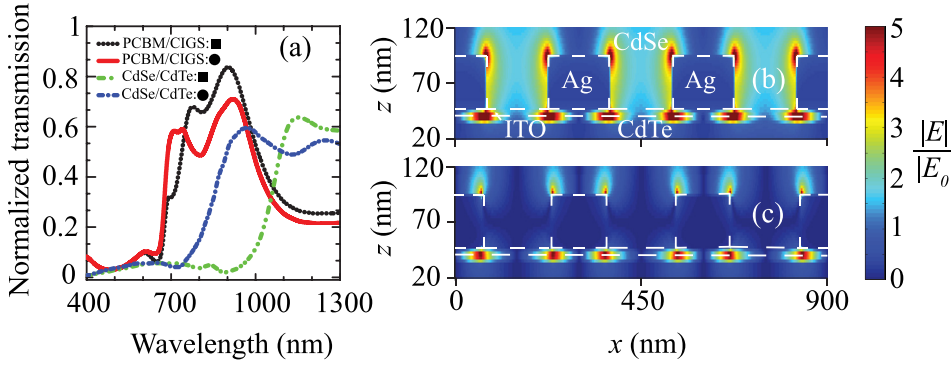
FIG. 12. (a) Normalized transmission spectra through a 2DHA with square and circle holes when the active materials are PCBM/CIGS and CdSe/CdTe. Normalized electric field profile ($|E|/|E_0|$) in the x-z plane through the center of the hole for TE-polarized incident light of (b) 1150 nm in square 2DHA and (c) 900 nm in circle 2DHA.

TABLE I. Parameter values for calculation of $J_{sc}$.[31,34–37]

| Parameter | PCBM | CIGS |
|---|---|---|
| Relative dielectric permittivity | 3.4 | 13.6 |
| Bandgap | 1.9 eV | 1.1 eV |
| Electron lifetime | $2 \times 10^{-7}$ s | $5.5 \times 10^{-9}$ s |
| Hole lifetime | $3 \times 10^{-6}$ s | $2 \times 10^{-7}$ s |
| Electron-hole pair capture rate | $6 \times 10^{-13}$ cm$^3$/s | $7.2 \times 10^{-10}$ cm$^3$/s |
| Electron capture coefficient | $2.8 \times 10^{-31}$ cm$^6$/s | $1 \times 10^{-30}$ cm$^6$/s |
| Hole capture coefficient | $9.9 \times 10^{-32}$ cm$^6$/s | $1 \times 10^{-30}$ cm$^6$/s |

the terminals as the diffusion length of the carriers is much longer than the thickness of the active material.[29] Therefore, first, we calculate the ideal $J_{sc}$ assuming that all photo-generated electron-hole pairs are collected at the terminals. We find that the ideal $J_{sc}$ is 11.52 mA/cm$^2$ and 14.18 mA/cm$^2$ for PCBM and CIGS layers, respectively, if the intermediate metal layer with a square 2DHA is used. By contrast, the ideal $J_{sc}$ is 7.10 mA/cm$^2$ and 14.22 mA/cm$^2$ for PCBM and CIGS layers, respectively, if the intermediate metal layer is not used. We note a ~20.5% increase in $J_{sc}$ when the intermediate metal layer is used.

However, the intermediate metal layer may introduce surface defects in the structure, which may induce recombination of photo-generated electron-hole pairs. Additionally, there may be recombination of the photo-generated electron-hole pairs by different radiative and non-radiative processes. Therefore, to calculate $J_{sc}$ in a non-ideal case, we solve the continuity equation of current that includes the generation rate of electron-hole pairs due to incident photons, the

recombination rate due to defects and impurities in surface and material, and the transport rate of electrons and holes to the terminals due to drift and diffusion.[30] The non-radiative recombination mechanisms dominate among the recombination rates in both PCBM and CIGS.[31–33] Therefore, we have included trap-assisted recombination, Auger recombination, and surface recombination in the calculation. A list of parameters used for the calculation is given in Table I. We find that since the active layers are very thin, trap-assisted recombination and auger recombination have insignificant effects on $J_{sc}$.

In Fig. 13(a), we show the absorption spectra of PCBM top and CIGS bottom subcells. In Fig. 13(b), we show the $J_{sc}$ in PCBM and CIGS with surface recombination velocity. We note that the $J_{sc}$ decreases as the surface recombination velocity increases. If the surfaces are not passivated well, then the decrease in current can be significant. However, even if we assume a value of $10^7$ cm/s for the surface recombination velocity, which is the maximum limiting value for most semiconductors,[31,34–37] we find that the $J_{sc}$ is 9.53 mA/cm$^2$ for PCBM and 13.67 mA/cm$^2$ for CIGS layers so that the total $J_{sc}$ is still 9% greater than the ideal total $J_{sc}$ of the solar cell without the intermediate layer. Although the light absorption is greater in PCBM than in CIGS, we note that the $J_{sc}$ is greater in CIGS than in PCBM. The coulombic interaction between electrons and holes in organic material PCBM is much greater than that in the direct bandgap inorganic material CIGS, which contributes to a significantly smaller carrier mobility in PCBM than that in CIGS.[34,35] As a result, the $J_{sc}$ in PCBM is smaller than that in CIGS despite a greater amount of photon absorption in PCBM.
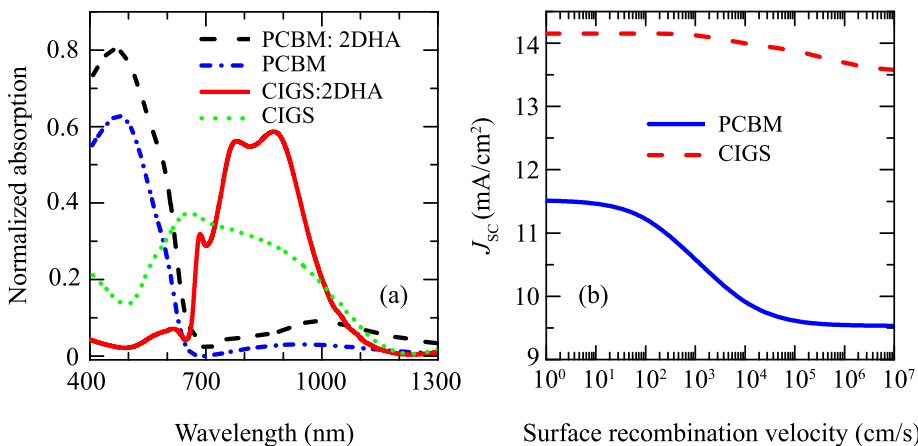


FIG. 13. (a) Normalized absorption spectra in a PCBM/CIGS ultra-thin-film tandem solar cell with and without 2DHA, (b) short circuit current density of active PCBM and CIGS layers as a function of surface recombination velocity. In each case, the geometry of the silver 2DHA is square, the thickness of 2DHA is fixed at 50 nm, and the area of square holes is fixed at 22 500 nm$^2$.

## VIII. CONCLUSION

In this work, we have investigated the role of EOT structures on ultra-thin-film tandem solar cells. We find that the excitation mechanism varies as the shape of holes in the metal layer varies. As a result, the transmission spectra through the 2DHA into the bottom subcell change. The performance of an ultra-thin-film solar cell with PCBM top and CIGS bottom subcells remains approximately the same when the holes are either a square or a regular polygon with a number of arms greater than 4. However, the performance suffers significantly when the holes are triangle. The transmission spectra can also be controlled by changing the dimensions of the holes in 2DHA. We have studied the effects of using different metals in the intermediate layer. We find that Ag will be the suitable metal to be used in the EOT based tandem solar cells mainly due to its low loss in the solar spectra. We have also investigated how EOT based structures work for different active materials in the top and bottom subcells. We find that the square and circle holes in a 2DHA produce approximately the same absorption in the top and bottom subcells when the materials are PCBM and CIGS in the top and bottom subcells, respectively. However, if CdSe and CdTe materials are used as the top and bottom subcells, respectively, the circle holes produce greater absorption in the subcells than that with the square holes. We also find that the $J_{sc}$ of an ultra-thin-film tandem solar cell with intermediate layer increases at least 9% from that when the intermediate layer is not used.

## ACKNOWLEDGMENTS

[1]See https://www.cia.gov/library/publications/the-world-factbook/rankorder/2233rank.html for electricity consumption of the world.

[2]N. S. Lewis, MRS Bull. **32**, 808–820 (2007).

[3]P. Bermel, C. Luo, L. Zeng, L. C. Kimerling, and J. D. Joannopoulos, Opt. Express **15**, 16986–17000 (2007).

[4]H. A. Atwater and A. Polman, Nat. Mater. **9**, 205–213 (2010).

[5]M. D. Kelzenberg, S. W. Boettcher, J. A. Petykiewicz, D. B. Turner-Evans, M. C. Putnam, E. L. Warren, J. M. Spurgeon, R. M. Briggs, N. S. Lewis, and H. A. Atwater, Nat. Mater. **9**, 239–244 (2010).

[6]M. Law, L. E. Greene, J. C. Johnson, R. Saykally, and P. D. Yang, Nat. Mater. **4**, 455–459 (2005).

[7]J. Zhu, C.-M. Hsu, Z. Yu, S. Fan, and Y. Cui, Nano Lett. **10**, 1979–1984 (2010).

[8]M. J. Naughton, K. Kempa, Z. F. Ren, Y. Gao, J. Rybczynski, N. Argenti, W. Gao, Y. Wang, Y. Peng, J. R. Naughton, G. McMahon, T. Paudel, Y. C. Lan, M. J. Burns, A. Shepard, M. Clary, C. Ballif, F. J. Haug, T. Soederstroem, O. Cubero, and C. Eminian, Phys. Status Solidi RRL **4**, 181–183 (2010).

[9]R. Biswas, J. Bhattacharya, B. Lewis, N. Chakravarty, and V. Dalal, Sol. Energy Mater. Sol. Cells **94**, 2337–2342 (2010).

[10]S. B. Mallick, M. Agrawal, and P. Peumans, Opt. Express **18**, 5691–5706 (2010).

[11]V. E. Ferry, M. A. Verschuuren, H. B. T. Li, E. Verhagen, R. J. Walters, R. E. I. Schropp, H. A. Atwater, and A. Polman, Opt. Express **18**, A237–A245 (2010).

[12]C. Eisele, C. E. Nebel, and M. Stutzmann, J. Appl. Phys. **89**, 7722–7726 (2001).

[13]C. Haase and H. Stiebig, Appl. Phys. Lett. **91**, 061116 (2007).

[14]D. Shir, J. Yoon, D. Chanda, J.-H. Ryu, and J. A. Rogers, Nano Lett. **10**, 3041–3046 (2010).

[15]M. A. Awal, Z. Ahmed, and M. A. Talukder, J. Appl. Phys. **117**, 063109 (2015).

[16]T. W. Ebbesen, H. J. Lezec, H. F. Ghaemi, T. Thio, and P. A. Wolff, Nature **391**, 667–669 (1998).

[17]S. G. Rodrigo, *Optical Properties of Nanostructured Metallic System Studied with Finite Difference Time-Domain Method* (Springer, 2012).

[18]M. Beruete, M. Sorolla, and I. Campillo, Opt. Express **14**, 5445–5455 (2006).

[19]M. Beruete, M. Sorolla, M. Navarro-Cia, F. Falcone, I. Campillo, and V. Lomakin, Opt. Express **15**, 1107–1114 (2007).

[20]R. Gordon, D. Sinton, K. L. Kavanagh, and A. G. Brolo, Acc. Chem. Res. **41**, 1049–1057 (2008).

[21]X. Zhang, Q. Huang, J. Hu, R. J. Knize, and Y. Lu, Opt. Express **22**, A1400–A1411 (2014).

[22]S. H. Demtsu and J. R. Sites, Thin Solid Films **510**, 320–324 (2006).

[23]H. Takato, M. Yamanaka, Y. Hayashi, R. Shimokawa, S. Hide, S. Gohda, F. Nagamine, and H. Tsuboi, Jpn. J. Appl. Phys., Part 2 **31**, L1665–L1667 (1992).

[24]M. W. Rowell and M. D. McGehee, Energy Environ. Sci. **4**, 131–134 (2011).

[25]R. Gordon and A. G. Brolo, Opt. Express **13**, 1933–1938 (2005).

[26]Q. Wang, J. Li, C. Huang, C. Zhang, and Y. Zhu, Appl. Phys. Lett. **87**, 091105 (2005).

[27]P. R. West, S. Ishii, G. V. Naik, N. K. Emani, V. M. Shalaev, and A. Boltasseva, Laser Photonics Rev. **4**, 795–808 (2010).

[28]R. W. Miles, G. Zoppi, and I. Forbes, Mater. Today **10**, 20–27 (2007).

[29]R. A. Pala, J. White, E. Barnard, J. Liu, and M. L. Brongersma, Adv. Mater. **21**, 3504–3509 (2009).

[30]S. L. Chuang, *Physics of Photonic Devices* (Wiley, 2009).

[31]M. A. Gloeckler, Ph.D. thesis, Colorado State University, 2005.

[32]A. Pivrikas, N. S. Sariciftci, G. Juska, and R. Osterbacka, Prog. Photovoltaics: Res. Appl. **15**, 677–696 (2007).

[33]R. A. Street, M. Schoendorf, A. Roy, and J. H. Lee, Phys. Rev. B **81**, 205307 (2010).

[34]F. Monestiera, J.-J. Simona, P. Torchioa, L. Escoubasa, F. Florya, S. Baillyb, R. de Bettigniesb, S. Guillerezb, and C. Defranoux, Sol. Energy Mater. Sol. Cells **91**, 405–410 (2007).

[35]M. I. Alonso, M. Garriga, C. A. D. Rincón, E. Hernández, and M. León, Appl. Phys. A **74**, 659–664 (2002).

[36]J. Schafferhansa, A. Baumanna, A. Wagenpfahla, C. Deibela, and V. Dyakonov, Org. Electron. **11**, 1693–1700 (2010).

[37]R. C. I. MacKenzie, C. G. Shuttle, M. L. Chabinyc, and J. Nelson, Adv. Energy Mater. **2**, 662–669 (2012).